CLIMATOLOGY

Eastward shift and extension of ENSO-induced tropical precipitation anomalies under global warming

Zixiang Yan[1,2], Bo Wu[1,3]*, Tim Li[2,4], Mat Collins[5], Robin Clark[6], Tianjun Zhou[1,3], James Murphy[6], Guirong Tan[2]

During El Niño events, increased precipitation occurs over the equatorial central eastern Pacific, corresponding to enhanced convective heating that modulates global climate by exciting atmospheric teleconnections. These precipitation anomalies are projected to shift and extend eastward in response to global warming. We show that this predicted change is caused by narrowing of the meridional span of the underlying El Niño–related sea surface temperature (SST) anomalies that leads to intensification of the meridional gradient of the SST anomalies, strengthening boundary-layer moisture convergence over the equatorial eastern Pacific, and enhancing local positive precipitation anomalies. The eastward shift and extension of these anomalies also intensify and extend eastward negative precipitation anomalies over the tropical western North Pacific, by strengthening equatorward advection of low mean moist enthalpy. Changes in El Niño–induced tropical precipitation anomalies suggest that, under global warming, El Niño events decay faster after their peak phase, thus shortening their duration.

INTRODUCTION

The El Niño–Southern Oscillation (ENSO), the strongest interannual variability signal in the climate system, is generated by air-sea interactions in the tropical Pacific (*1*–*5*). ENSO-driven convective heating anomalies over the tropical Pacific influence global climate system and thus extreme weather events, agriculture, and ecosystem around the world through atmospheric teleconnections (*4*, *6*–*9*).

Global climate model (GCM) projections suggest that ENSO intensity could be highly sensitive to planetary scale future warming (*10*, *11*). Uncertainties though, due to incomplete knowledge about forcing and feedback processes, are large (*10*–*18*). However, despite these uncertainties, projected changes in ENSO-driven precipitation anomalies are surprisingly robust, with intensification of both positive and negative anomalies over the equatorial central eastern Pacific (CEP) and tropical western Pacific, respectively (*19*–*24*). From this perspective, ENSO intensity will increase under global warming, both within the Pacific (*19*, *20*) and beyond (*25*, *26*). The ENSO-driven precipitation changes have been attributed to the warming of background mean sea surface temperature (SST) and associated changes in the atmospheric circulations and moisture (*19*, *20*, *27*), as well as changes in ENSO-related circulation anomalies due to pattern changes in background SST and ENSO-related SST anomalies (*20*–*23*).

In addition to the intensity changes, ENSO-driven positive precipitation anomalies over the equatorial Pacific were projected to be shifted and extended eastward (*19*–*22*) and thus lead to eastward shifts of the dominant variability mode of the Walker circulation (*28*) and the atmospheric teleconnection pattern over the North Pacific and North America forced by ENSO (*29*–*33*). However, the causation of this shift and extension has remained unexplained. In this study, we demonstrate that the change in ENSO-driven precipitation anomalies results from the narrowing of the meridional span of ENSO-related positive SST anomalies based on a 57-member earth system parameter-perturbed ensemble conducted with the state-of-the-art GCM HadCM3C (hereafter ESPPE; Materials and Methods).

RESULTS

During El Niño mature winters [December(0)-January-February(1), when El Niño events typically peak], the tropical Pacific is dominated by a dipole of positive and negative precipitation anomalies over the equatorial CEP and tropical western Pacific (*11*, *34*), respectively, corresponding to the eastward shift of the Walker circulation caused by changes in the zonal gradient of SST in the equatorial Pacific. The historical simulations from the ESPPE reproduce these features (Fig. 1, A and D) well, with overall simulation skill notably higher than that of the multimodel ensemble from the phase 5 of the Coupled Model Intercomparison Project (CMIP5) (fig. S1), partly due to its high skill in background mean states (figure not shown) (*35*–*37*). Meanwhile, member spreads in simulation skill from the ESPPE and CMIP5 are comparable (fig. S1). The encouraging skill of the ESPPE suggests that it is suitable for examining projections of future ENSO-driven precipitation.

For the climate projections under the representative concentration pathway (RCP) 8.5 scenario (hereafter RCP8.5 simulations) from the ESPPE, the ENSO-driven precipitation anomalies over both the equatorial CEP and tropical western North Pacific (WNP) are greatly intensified (Fig. 1B). The center of the positive anomalous precipitation over the equatorial CEP is displaced eastward by approximately 10° with a concomitant extension of its tail (Fig. 1B). As a result, the difference in the precipitation anomalies between the RCP8.5 and historical simulations (ΔPr′) shows a zonal dipole pattern, with a positive pole centered close to 150°W and along the equator and a

[1]State Key Laboratory of Numerical Modeling for Atmospheric Sciences and Geophysical Fluid Dynamics (LASG), Institute of Atmospheric Physics, Chinese Academy of Sciences, Beijing, China. [2]Key Laboratory of Meteorological Disaster, Ministry of Education/Joint International Research Laboratory of Climate and Environmental Change/Collaborative Innovation Center on Forecast and Evaluation of Meteorological Disasters, Nanjing University of Information Science and Technology, Nanjing, China. [3]CAS Center for Excellence in Tibetan Plateau Earth Sciences, Chinese Academy of Sciences (CAS), Beijing, China. [4]International Pacific Research Center (IPRC), and Department of Atmospheric Sciences, SOEST, University of Hawaii at Manoa, Honolulu, HI 96822, USA. [5]College of Engineering Mathematics and Physical Sciences, University of Exeter, Harrison Building, Streatham Campus, Exeter, EX4 4QF, UK [6]Met Office Hadley Centre, FitzRoy Road, Exeter Ex1 3PB, UK.
*Corresponding author. Email: wubo@mail.iap.ac.cn

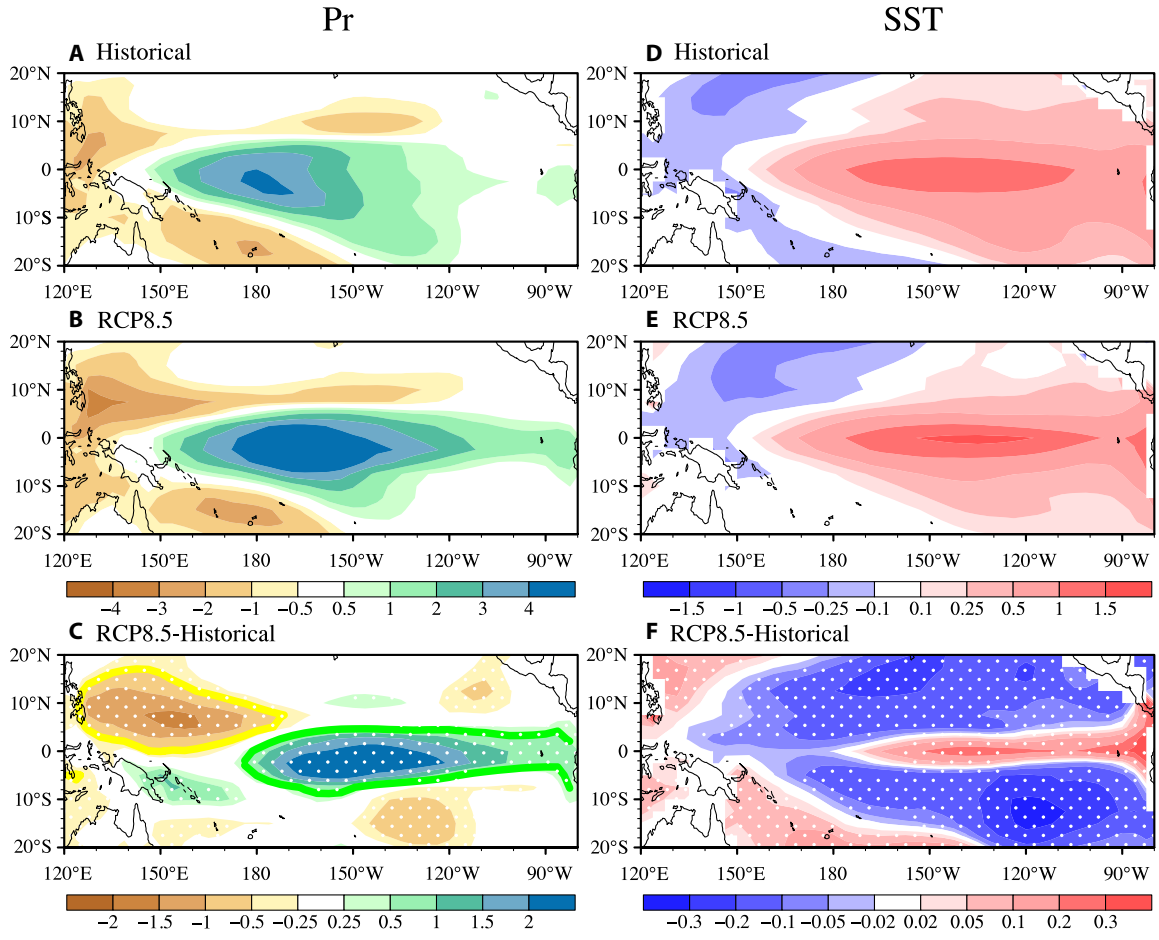

Fig. 1. Simulated changes in the ENSO-driven D(0)JF(1)-mean precipitation and SST anomalies under global warming. (**A** and **B**) Ensemble-mean ENSO-driven precipitation anomalies for the historical and RCP 8.5 simulations, respectively. (**C**) Differences between (A) and (B). A Student's *t* test is conducted for the change in precipitation and SST anomalies. Values reaching 5% significance level are dotted. Yellow (green) line denotes the area where change in precipitation anomalies is less than −0.5 mm day^{-1} (greater than 0.5 mm day^{-1}). (**D** to **F**) As in (A) to (C), but for ENSO-related SST anomalies.

negative pole centered at 155°E, 6°N (Fig. 1C). Here, the precipitation anomalies are regressed onto the original (unnormalized) Niño3.4 index time series for both the historical and RCP8.5 simulations, respectively (Materials and Methods). Thus, the obtained ENSO-driven precipitation anomalies correspond to 1°C Niño3.4 index for both simulations. A change in precipitation anomalies driven by changes in ENSO SST amplitude is excluded in consideration of the large uncertainties and controversies in the ENSO amplitude change (*10*–*18*, *38*).

In contrast to the zonal dipole pattern of the ΔPr′, a change is seen in the structure of the ENSO-related SST anomalies. For ENSO events of similar Niño3.4 indices, warm SST anomalies in the equatorial CEP in the RCP8.5 simulations significantly shrink toward equator relative to that in the historical simulations (Fig. 1, D and E). Correspondingly, differences in the ENSO-related SST anomalies between the two simulations (ΔSST′) show a sandwich structure in the CEP, with a very narrow positive band along the equator, bounded by negative values on both sides (Fig. 1F).

To investigate the mechanisms responsible for the dipole pattern of the ΔPr′, we diagnose the moisture budgets for the positive and negative poles, respectively (Materials and Methods). The change in the precipitation anomalies (ΔPr′) is mainly caused by the change in vertically integrated vertical advection of climatological moisture by anomalous vertical motions ($\Delta\langle-\omega'\partial_p\overline{q}\rangle$) for both the domains (fig. S2). $\Delta\langle-\omega'\partial_p\overline{q}\rangle$ can be decomposed into two linear components, $\langle-\Delta\omega'\partial_p\overline{q}\rangle$ and $\langle-\omega'\partial_p\Delta\overline{q}\rangle$ (fig. S3), associated with the changes in ENSO-related vertical motion anomalies (Δω′) and background climatological mositure ($\Delta\overline{q}$), respectively.

The positive ΔPr′ over the equaotiral CEP is dominated by the $\langle-\Delta\omega'\partial_p\overline{q}\rangle$ component (fig. S3B), indicating that the eastward shift and extension of the ENSO-driven positive precipitation anomalies are mainly caused by the change in ENSO-driven upward motion anomalies ($\langle-\Delta\omega'\partial_p\overline{q}\rangle$). On the other hand, the positive $\langle-\omega'\partial_p\Delta\overline{q}\rangle$ is confined in the equatorial central Pacific (fig. S3C), suggesting that the increase in mean moisture due to global warming has a moderate contribution to the intensification of the ENSO-driven positive precipitation anomalies in situ but almost no contribution to their eastward shift and extension.

To understand the change in the three-dimensional anomalous vertical motions (Δω′), we simplify the problem by separating its horizontal distribution from the vertical structure. In the tropics, vertical motions can be approximately described as two vertical modes, deep and shallow modes (Ω_d and Ω_s) (Materials and Methods) (*39*, *40*).

Vertical profiles of both modes show bow structures, with the former being top-heavy and nearly having no boundary-layer convergence between 850 hPa and surface, while the latter being bottom-heavy and having a strong boundary-layer convergence (right panels of Fig. 2, B and C, and fig. S4, B and C). For both the historical and RCP8.5 simulations, the two modes account for about 77% of the total variances of vertical profiles of horizontal convergence in the tropics. On the basis of the two modes, the $\langle -\Delta\omega'\partial_p\overline{q}\rangle$ component can be further decomposed into two subcomponents, $-\Delta\sigma_d'\langle\Omega_d\partial_p\overline{q}\rangle$ and $-\Delta\sigma_s'\langle\Omega_s\partial_p\overline{q}\rangle$, associated with the changes in the deep- and shallow-mode amplitudes ($\Delta\sigma_d'$ and $\Delta\sigma_s'$), respectively (Fig. 2, B and C, and Materials and Methods). The two subcomponents have nearly equal contributions to the magnitude of the positive pole of $\Delta Pr'$ (fig. S2A, right). However, the $-\Delta\sigma_s'\langle\Omega_s\partial_p\overline{q}\rangle$ associated with the change in the shallow-mode amplitude dominates the eastward shift and extension of the ENSO-driven positive precipitation anomalies (Fig. 2C).

Shallow-mode vertical motions are tightly linked to boundary-layer convergence patterns, the formation of which can be understood through an analytical mixed layer model (Supplementary Materials and Methods) (*41*). Surface wind anomalies and associated convergence anomalies are driven by both free-tropospheric and boundary-layer processes, which can be distinguished by decomposing surface pressure anomalies into free-tropospheric (above mean height of 850 hPa) and boundary-layer components (Supplementary Materials and Methods, contours in fig. S5) (*41*). It is found that the change in the latter (hereafter P_{BL}) dominates the change in the surface convergence anomalies over the equatorial CEP (fig. S5).

The P_{BL} gradient can be simplified as a function of the SST, assuming that the boundary layer's air temperature varies linearly from the surface to the top of the boundary layer (mean height of

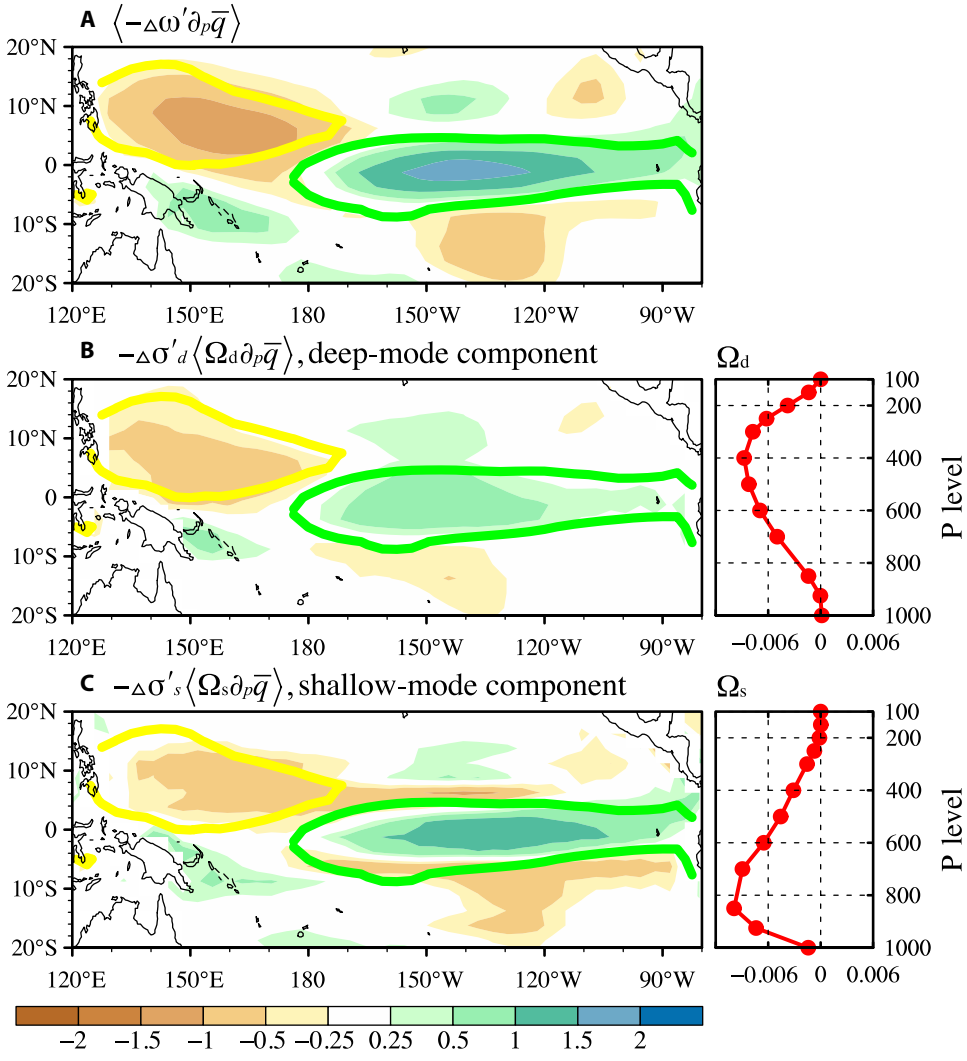

Fig. 2. Simulated changes in the ENSO-driven tropical precipitation anomalies due to change in vertical motion anomalies under global warming. (**A**) Vertically integrated vertical advection of climatological specific humidity by the differences in anomalous vertical motions between the RCP8.5 and the historical simulations, averaged over the ESPPE members. (**B** and **C**) Contributions of changes in deep- and shallow-mode amplitudes to that shown in (A), respectively. Red lines attached to the right of (B) and (C) are the normalized vertical profiles of the deep and shallow modes, respectively. Thick yellow and green lines denote the area where change in precipitation anomalies is less than −0.5 mm day^{-1} (greater than 0.5 mm day^{-1}), as shown in Fig. 1C.

850 hPa), and the 850 hPa temperature anomalies are uniform (horizontal gradients are zero). A theoretical model similar to the classical Lindzen-Nigam model (LN-like model) (*42*) can then be constructed for understanding the simulations from the ESPPE, in which only the simulated SST is specified as an input (Supplementary Materials and Methods). The meridional sandwich-like structure of the boundary-layer convergence can be reproduced by the LN-like model (Fig. 3, A and B). The structure corresponds to an underlying hill-shaped meridional structure of zonal-averaged SST anomalies over the CEP, which reaches maximum on the equator and has steepest gradients between 5°N and 5°S (Fig. 3C). Furthermore, the magnitudes of divergence of ΔSST′ gradient ($\frac{\partial^2}{\partial y^2}(\Delta SST')$) and surface convergence anomalies in the positive pole domain are calculated for individual members. Their correlation reaches −0.83 (Fig. 3D). These results indicate that the meridional narrowing of ENSO-related SST anomalies intensifies boundary-layer convergence anomalies over the equatorial CEP and thus enhances the shallow-mode upward motion anomalies, which are responsible for the eastward shift and extension of ENSO-driven positive precipitation anomalies.

The meridional width of ENSO is associated with the strength of poleward advection of oceanic temperature anomalies from the equator by mean meridional overturning circulation of the subtropical cell (STC) (*43*–*48*). The simulated STC is weakened by 30% under global warming, as a response to the robust weakening of the mean easterly trade wind over the equatorial CEP (Fig. 4) (*48*, *49*). The weakened mean STC causes the narrowing of ENSO meridional width and further forces stronger boundary-layer convergence anomalies over the equatorial eastern Pacific, even if ENSO amplitude does not vary.

In addition to the change in the shallow-mode amplitude, the increase in the deep-mode amplitude also has a contribution to the intensification of ENSO-driven positive precipitation anomalies over the equatorial CEP (Fig. 2B). In the tropics, deep-mode vertical motion is constrained by moist static energy (MSE) budget in the atmospheric column (*50*). We diagnose the change in the MSE budget between the two simulations (Materials and Methods). The results indicate that the increase in the amplitude of deep-mode upward motion anomalies in the positive pole is dominated by the increase in ENSO-related net MSE flux anomalies from top of atmosphere and surface ($\Delta F'_{\mathrm{net}}$; fig. S6, A and B), while changes in the background mean states under global warming including vertical stratification of mean MSE ($\langle -\omega' \partial_p \Delta \overline{h} \rangle$) and mean upward motion ($\langle -\Delta\overline{\omega} \partial_p h' \rangle$) play secondary roles (figs. S6A and S7, C and D). $\Delta F_{\mathrm{net}}{}'$ is mainly caused by the increase in ENSO-driven cloud longwave radiative flux anomalies ($\Delta R'_{\mathrm{cloud}}$). The cloud longwave radiative flux anomalies are associated with the convection-cloud-longwave radiation feedback, an internal positive feedback in the tropical atmosphere, which just further amplifies ΔPr′ but does not change its spatial pattern (contours in fig. S7B).

We now turn to focus on the formation of the negative pole of ΔPr′ over the tropical WNP (yellow contour in Fig. 1C). The negative ΔPr′ is caused by the strengthening of ENSO-related descending anomalies over the tropical WNP under global warming, while the increase in the background mean moisture almost has no contribution (fig. S3). Further decomposition of the vertical motion anomalies into deep and shallow modes indicates that the amplitude changes in the two modes have approximately equal contributions (Fig. 2 and fig. S2B). The strengthening of the shallow-mode amplitude is not caused by the change in underlying SST anomalies gradient as the case for the positive pole (Fig. 3, A and B) but mainly by free-tropospheric processes including horizontal temperature gradient on top of the boundary layer and downward momentum mixing (fig. S5). It suggests that the change in the boundary-layer convergence anomalies and associated shallow-mode amplitude is driven by intensified local anomalous descending motion (suppressed deep convections) associated with the change in the deep-mode amplitude.

The deep-mode amplitude is constrained by the MSE budget, as noted above. The suppressed convection over the tropical WNP during El Niño mature winter is primarily driven by negative horizontal advection of mean moist enthalpy by anomalous northerly anomalies ($\langle -\vec{u}' \nabla_h \overline{k} \rangle$) to the western flank of cyclone anomalies stimulated by the positive precipitation anomalies over the equatorial CEP, which is referred to as anomalous wind-moist enthalpy advection mechanism (*34*, *51*). Under global warming, the change in $\langle -\vec{u}' \nabla_h \overline{k} \rangle$ term is dominated by $\langle -\Delta\vec{u}' \nabla_h \overline{k} \rangle$ associated with the change in ENSO-driven wind anomalies (fig. S8). The positive ΔPr′ in the equatorial CEP drives a cyclonic change in low-level circulation anomalies to the west in terms of the Gill model. The northerly component to the western flank of the cyclone transports air with low mean moist enthalpy to the tropical WNP and thus strengthens the negative anomalous wind-moist enthalpy advection, which are responsible for the enhanced descending anomalies and negative ΔPr′ (fig. S8B).

The physical processes responsible for the change in the ENSO-driven tropical precipitation anomalies under global warming are summarized as follows: The weakened climatological STC associated with the weakened mean easterly trade wind leads to a meridional narrowing of ENSO-related warm SST anomalies by reducing poleward advection of anomalous warm water from the equator. This narrowing leads to stronger meridional temperature gradient anomalies, which enhance the ENSO-driven boundary-layer convergence anomalies over the equatorial CEP. This process plays a key role in the eastward shift and extension of ENSO-driven positive precipitation anomalies over the CEP. In addition, the changes in the mean states, including moisture content, vertical motions, and vertical stratification of MSE, and positive convection-cloud-longwave radiation feedback have contributions to the intensification of the ENSO-driven positive precipitation anomalies. The change in the positive precipitation anomalies over the CEP stimulates a cyclonic change in low-level wind anomalies to the west. The northerly component to the western flank of the cyclone intensifies ENSO-driven negative precipitation anomalies over the tropical WNP by enhancing advection of low climatological moist enthalpy from the subtropics (schematic diagram in Fig. 5).

We also checked the results of the 31 CMIP5 models, which support the mechanism from the ESPPE, namely, that the change in the ENSO-driven precipitation anomalies over the CEP is modulated by the underlying meridional span of the ENSO-related SST anomalies. In ensemble mean of the 31 CMIP5 models, the change in ENSO-driven positive precipitation anomalies over the equatorial CEP between RCP8.5 and historical runs (ΔPr′) corresponds to the eastward shift and extension of the positive precipitation anomalies, similar to that in the ESPPE (fig. S9C and Fig. 1C). For all these models, the changes in the underlying surface convergence anomalies are highly correlated with the change in divergence of meridional gradient of the underlying SST anomalies, with their correlation coefficient reaching −0.85 (fig. S10).

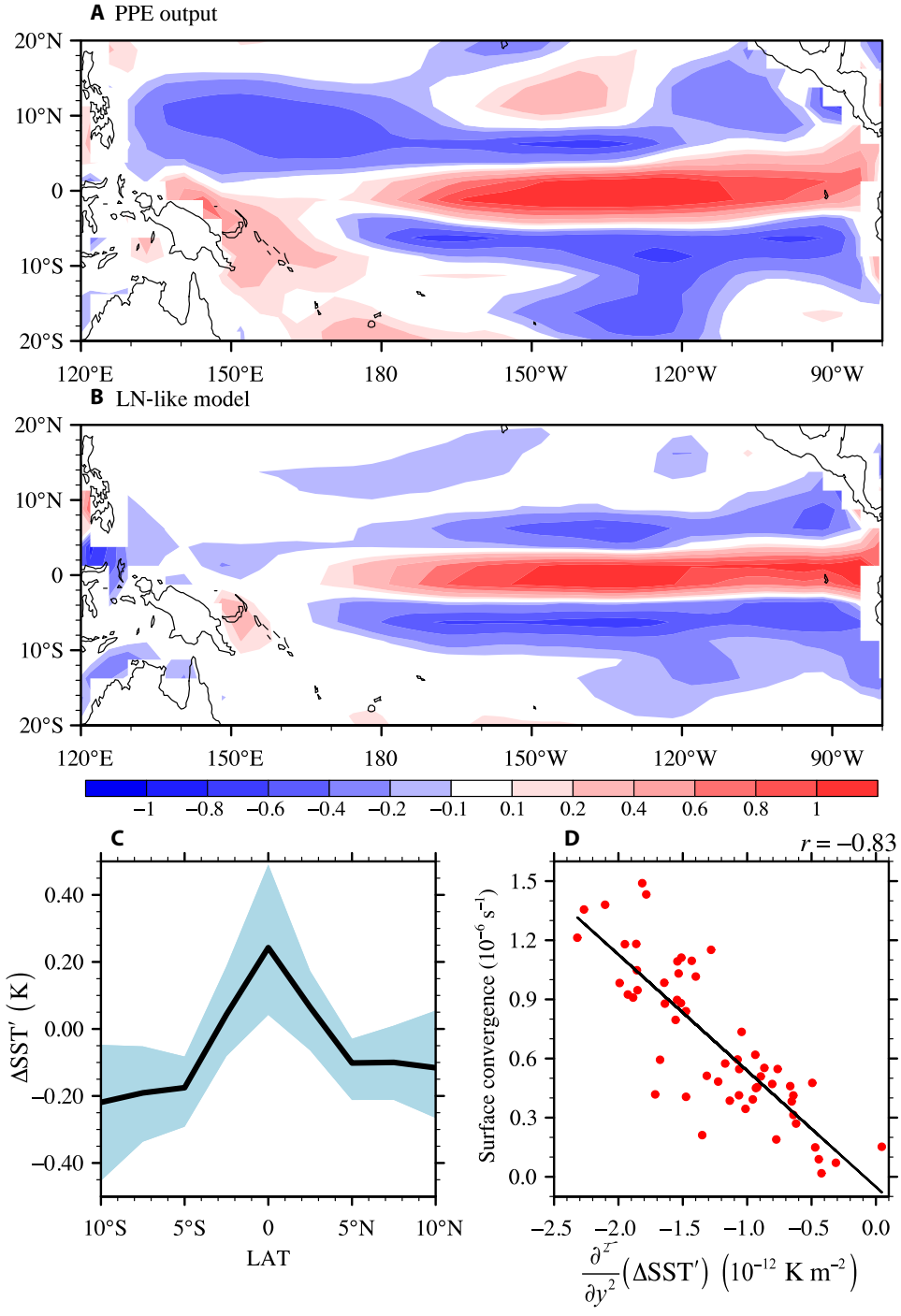

Fig. 3. Simulated changes in ENSO-driven surface convergence anomalies under global warming. (**A**) Differences in surface convergence (shading, 10^{-6} s^{-1}) anomalies between the RCP8.5 and historical simulations, averaged over the ESPPE members. (**B**) As in (A), but from the LN-like model driven by the simulated changes in SST anomalies only. (**C**) Meridional distribution of the differences in SST anomalies between two simulations zonally averaged over 155° to 110°W. Thick line shows the ensemble mean of the ESPPE. The light blue shading is the spread corresponding to 5th to 95th percentiles. (**D**) Scatter diagram for changes in divergence of meridional gradient of SST anomalies averaged in 4°N to 4°S, 155° to 110°W (ordinate axis) versus change in local surface convergence anomalies (abscissa axis). Their correlation coefficient is noted on the upper right corner.

The changes in the ENSO-driven precipitation anomalies have great climate impacts globally. First, the eastward shift and extension of the positive precipitation anomalies lead to the eastward shift of the Pacific–North American teleconnection pattern, thus the change in ENSO impacts on the North American winter temperature (Fig. 6A) (*29*–*33*). Second, they lead to the eastward shift

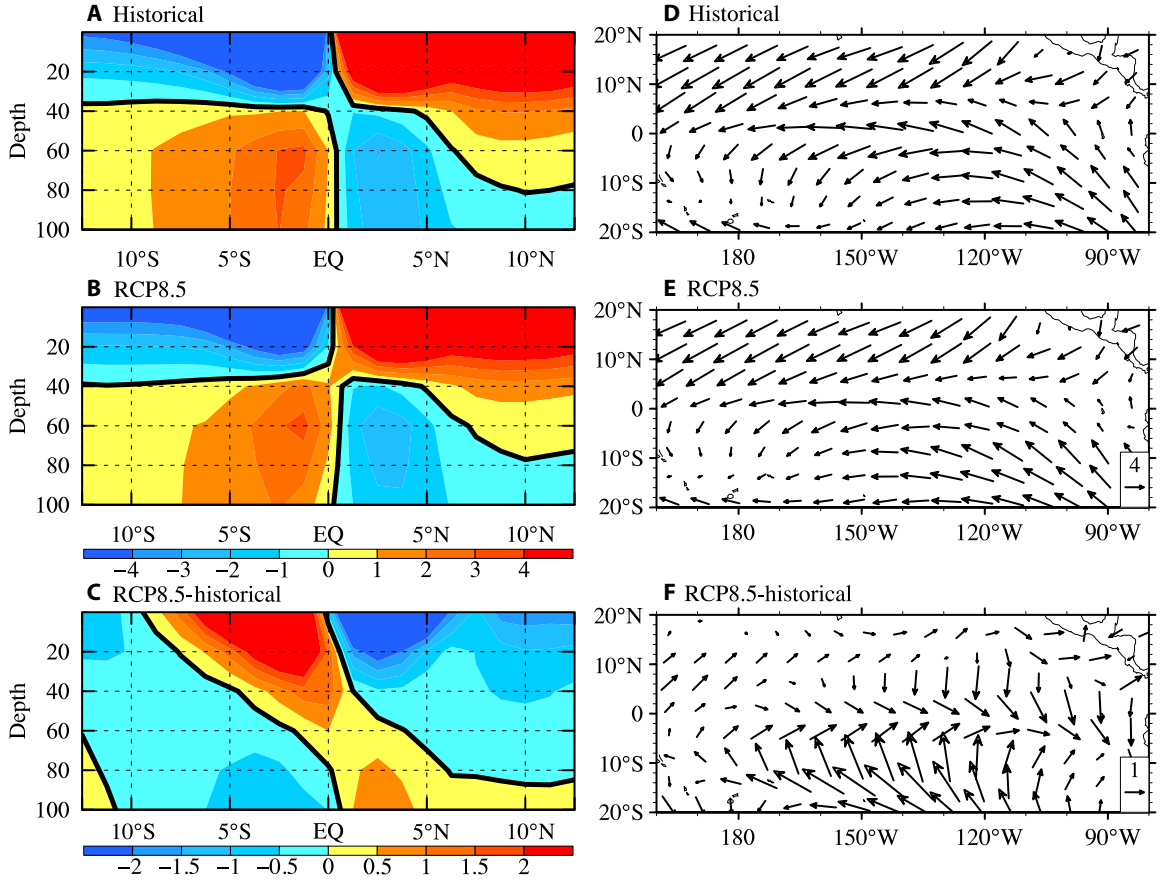

Fig. 4. Simulated changes in climatological STC and surface wind under global warming. (**A** and **B**) Longitude-depth plots for ensemble-mean climatological meridional ocean current (10^{-2} m s^{-1}) in D(0)JF(1) averaged over 160°E to 90°W for the historical and RCP 8.5 simulations, respectively. (**C**) Differences between (A) and (B). (**D** to **F**) As in (A) to (C), but for horizontal distribution of climatological 10-m wind (m s^{-1}).

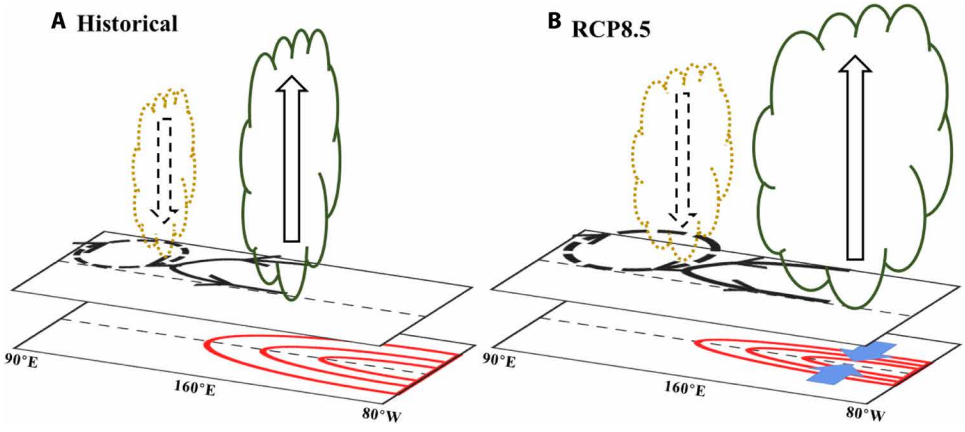

Fig. 5. Schematic diagram illustrating the physical processes responsible for the eastward shift and extension of ENSO-induced tropical precipitation anomalies under global warming. (**A**) Historical simulation; (**B**) RCP8.5 simulation.

of ENSO-driven anomalous Walker circulation (Fig. 6B), which is associated with the eastward shift of the dominant variability mode of the Walker circulation (*28*). Third, the negative ΔPr′ over the tropical WNP strengthens WNP anomalous anticyclone (WNPAC) during El Niño mature winter (Fig. 6C). The strengthened WNPAC leads to southeastern China becoming wetter in El Niño winter under global warming by transporting more moisture northward (Fig. 6). Meanwhile, the easterly anomalies to the southern flank of the WNPAC are intensified (Fig. 6C). The equatorial easterly wind anomalies stimulate eastward-propagating oceanic upwelling Kelvin waves, which contribute to the decay of El Niño (*52*–*56*). The intensified equatorial easterly anomalies tend to accelerate the decay of El Niño, which shorten its duration (Fig. 6, C and D).

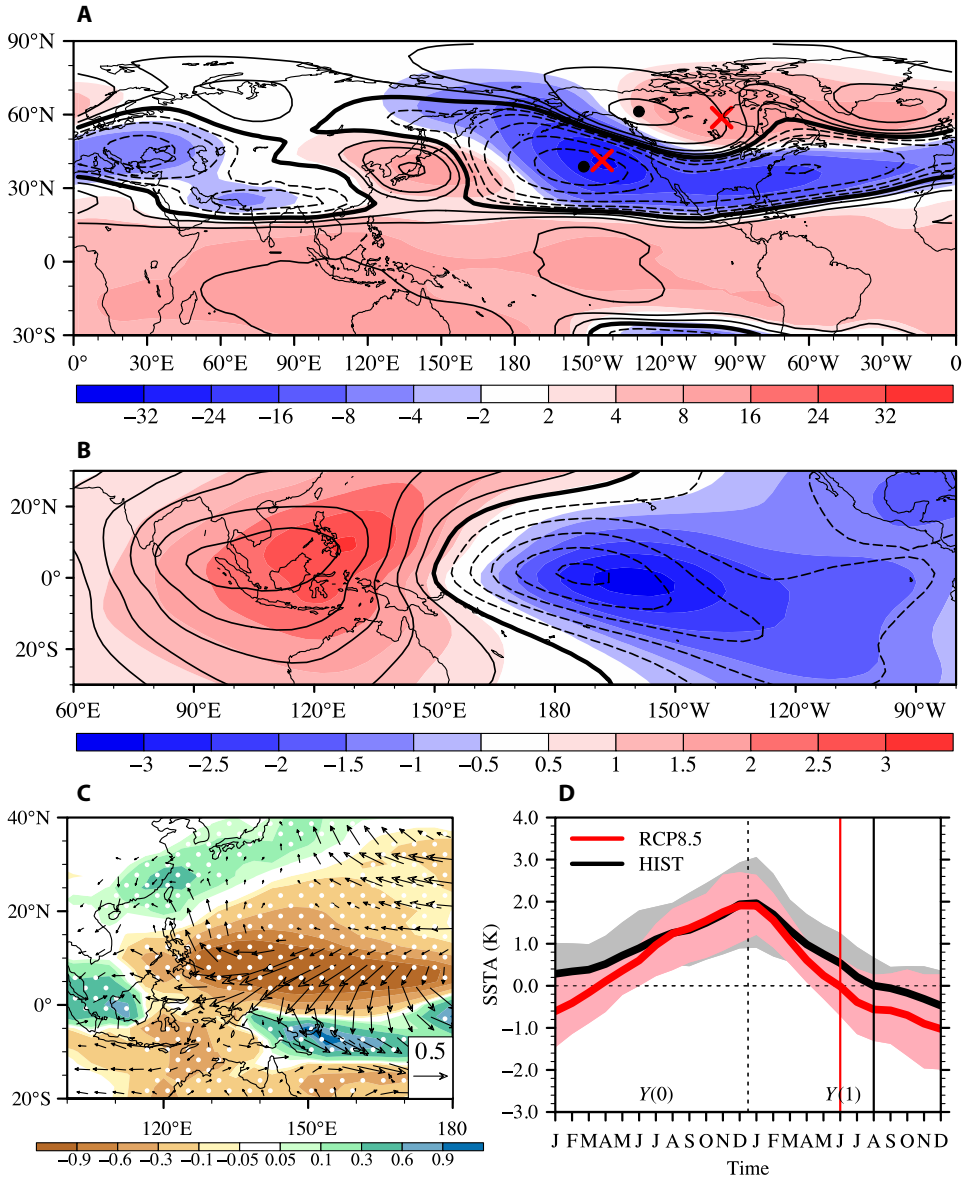

Fig. 6. Global climate impacts caused by the changes in the ENSO-driven precipitation anomalies. (**A**) Ensemble mean of ENSO-related D(0)JF(1)-mean 500-hPa geopotential height anomalies (m) for the historical (contour) and RCP8.5 simulations (shading). Black dots and red crosses denote the centers of geopotential height anomalies in historical and RCP8.5 simulations, respectively. (**B**) As in (A), but for 200-hPa velocity potential anomalies (10^6 m^2 s^{-1}). (**C**) Simulated changes in ENSO-driven precipitation anomalies (shading; mm day^{-1}) and 925-hPa wind anomalies (vector; m s^{-1}) under global warming. Values reaching 5% significance level are dotted. (**D**) Temporal evolutions of Niño3.4 indices for El Niño events in the historical (black) and RCP8.5 (red) simulations. Thick lines denote ensemble means. Shadings denote 5th to 95th percentiles. Thin vertical lines denote the timing when Niño3.4 index transforms from positive to negative.

DISCUSSION

In summary, this study attributes the change in the ENSO-induced precipitation anomalies over the equatorial CEP under the global warming to the change in the meridional span of the ENSO-related SST anomalies based on the ESPPE. The ESPPE shows that mean STC would weaken under the global warming, corresponding to the narrowing of the ENSO-related SST anomalies, which is consistent with theoretical model results (*47*). In addition, we cannot rule out the possibility that the narrowing of the ENSO-related SST anomalies, in turn, is also contributed by the change in the overlying precipitation anomalies. These open questions deserve further study in the future.

MATERIALS AND METHODS

Model and experiments

This study is based on the ESPPE, a large ensemble of climate simulations produced by the HadCM3C model developed by the Met Office Hadley Centre. The HadCM3C is a state-of-the-art coupled GCM, with the regular resolutions of 2.5° × 3.75° and 1.25° × 1.25° in the atmospheric and oceanic components, respectively (*57*, *58*). The ensemble has 57 members from different model versions, generated by simultaneously perturbing prescribed combinations of multiple parameters in the atmosphere, ocean, sulfur cycle, and terrestrial ecosystem components of HadCM3C. In the atmospheric component, 30 parameters were perturbed including, for example,

the relative humidity threshold required for cloud formation, cloud droplet to rain conversion rates, and surface roughness lengths. In the ocean component, perturbed parameters included those controlling the horizontal mixing of heat and momentum and the penetration of shortwave fluxes into the ocean. Sulfur cycle parameter perturbations were designed to model uncertainties in the conversion of SO_2 to sulfate aerosols and their removal. Ecosystem component parameters included perturbations to the rate of soil respiration and factors controlling the sensitivity of plant stomata to atmospheric CO_2. Details about the spinning up processes and perturbed parameter combinations can be found in (*59*). Standard CMIP5 historical and RCP8.5 simulations were used in this study. We use the simulations from the model years 1951–2000 and 2047–2096 following historical and RCP8.5 emission pathways, respectively.

Analysis processes

Model results were analyzed through the following steps. First, model variables in December(0)-January-February(1) [D(0)JF(1)] were detrended. Second, ENSO-related anomalies were obtained by regressing detrended variables onto D(0)JF(1)-mean Niño3.4 index (area-averaged SST anomalies in 5°N to 5°S, 170° to 120°W) for the historical and RCP8.5 simulations, respectively. Third, the difference in an ENSO-related anomaly between the RCP8.5 and historical simulations represented its change under global warming (denoted by Δ). Analyses were conducted for each ensemble member, and then ensemble means were calculated. Significances of ensemble-mean differences between the two simulations were tested by Student's *t* test.

Moisture and MSE equation diagnosis

Neglecting the small time-scale tendency term ($\partial t\langle q\rangle'$), the linearized anomalous moisture equation can be written as

$$P' = E' - \langle\overline{\vec{u}}\,\nabla_h q'\rangle - \langle\vec{u}'\,\nabla_h\overline{q}\rangle - \langle\overline{\omega}\,\partial_p q'\rangle - \langle\omega'\,\partial_p\overline{q}\rangle + \mathrm{NL} \quad (1)$$

where the prime signifies a detrended seasonal anomaly, the bar signifies a climatological mean state, and the angle bracket signifies a mass integral from the surface to 100 hPa. Here, P is the precipitation; E is the evaporation; $\vec{u}$ and ω are the horizontal wind and the vertical pressure velocity, respectively; and q is the specific humidity. NL represents all nonlinear and transient terms.

Similarly, by neglecting the time tendency of anomalous MSE, the linearized anomalous MSE equation can be written as

$$\langle\omega'\,\partial_p\overline{h}\rangle = F'_{\mathrm{net}} - \langle\overline{\vec{u}}\,\nabla_h k'\rangle - \langle\vec{u}'\,\nabla_h\overline{k}\rangle - \langle\overline{\omega}\,\partial_p h'\rangle + \mathrm{NL} \quad (2)$$

where MSE is $h = c_pT + L_vq + \Phi$ and moist enthalpy is $k = c_pT + L_vq$. T is the air temperature; c_p and L_v are the specific heat at constant pressure and the latent heat of vaporization, respectively; and Φ is the geopotential. F_{net} is the net MSE flux coming into the atmospheric column from the surface and the top of atmosphere. Detailed deviation of the anomalous MSE equation can be found in (*34*, *60*).

Changes in the moisture (MSE) budget under global warming were calculated as the difference in Eq. 1 (Eq. 2) between RCP8.5 and historical simulations. For both the moisture and MSE equations, changes in advection terms under global warming can be decomposed into two linear components, which are associated with changes in circulations and state variables, respectively. For example

$$\Delta\langle\omega'\partial_p\overline{h}\rangle \approx \langle\Delta\omega'\partial_p\overline{h}\rangle + \langle\omega'\partial_p\Delta\overline{h}\rangle \quad (3)$$

Deep and shallow modes of vertical motion profiles

Following (*40*), we obtained the deep and shallow modes of tropical vertical motions and associated horizontal convergences by following three steps. First, by applying a principal components analysis (PCA) on horizontal convergence profiles over tropical oceans (20°S to 20°N) in the historical simulations, we extracted the first two dominant modes (fig. S4A). Second, the two orthogonal modes were linearly combined to construct two new orthogonal basis modes under the condition that only one basis has projection on the near-surface (below 925 hPa) convergences (fig. S4B). The new mode having no (strong) surface convergence is referred to as a deep (shallow) mode. Third, the amplitudes of the deep and shallow modes (σ_d and σ_s) were calculated for the historical and RCP8.5 simulations, respectively. The vertical motion profiles associated with the deep and shallow modes (Ω_d and Ω_s) were subsequently computed by integrating the horizontal convergence downward from 100 hPa, at which vertical motion was assumed to be zero. Vertical velocity on the mean surface pressure was set to zero, and the integration residual was redistributed between the surface pressure and 100 hPa to satisfy mass continuity (fig. S4C). Hence, anomalous three-dimensional vertical motion can be approximately described by the two modes and written as

$$\omega'(x,y,p) \approx \sigma'_s(x,y)\cdot\Omega_s(p) + \sigma'_d(x,y)\cdot\Omega_d(p) \quad (4)$$

Considering that the vertical structures of the deep and shallow modes vary less under global warming (fig. S4C), from Eq. 4, the change in vertical advection of a state variable by anomalous vertical motion caused by the change in the anomalous vertical motion can be further decomposed into two subcomponents associated with amplitude changes in deep and shallow modes, respectively. For example, the first term on the right-hand side of Eq. 3 can be decomposed as

$$\langle\Delta\omega'\partial_p\overline{h}\rangle \approx \Delta\sigma'_d\langle\Omega_d\partial_p\overline{h}\rangle + \Delta\sigma'_s\langle\Omega_s\partial_p\overline{h}\rangle \quad (5)$$

The deep-mode vertical motion was mainly constrained by the MSE budget (*50*). Then, the equation for the change in MSE budget can be written as

$$\begin{aligned}\Delta\sigma'_d\langle\Omega_d\partial_p\overline{h}\rangle \approx -\Delta\sigma'_s\langle\Omega_s\partial_p\overline{h}\rangle - \langle\omega'\partial_p\Delta\overline{h}\rangle - \\ \Delta\langle\overline{\omega}\partial_p h'\rangle - \Delta\langle\overline{\vec{u}}\nabla_h k'\rangle - \Delta\langle\vec{u}'\nabla_h\overline{k}\rangle + F'_{\mathrm{net}} + \mathrm{NL}\end{aligned} \quad (6)$$

Selection of strong El Niño and La Niña events

Empirical orthogonal function analyses were applied to the monthly tropical Pacific SST anomalies (20°S to 20°N, 120°E to 80°W) for each ESPPE member. Strong El Niño events were selected on the basis of the criteria that (i) D(0)JF(1)-mean PC time series are greater than 1 SD (*61*) and (ii) the time series of Niño3.4 index reach the maximum between October(0) and March(1) in two consecutive years. Considering that La Niña events tend to maintain in two consecutive years, much longer than the El Nino events, the La Niña events were selected on the basis of one more criterion; that is, the PC1 index in preceding winter [D(−1)JF(0)] is larger than −0.5 SD.

SUPPLEMENTARY MATERIALS

Supplementary material for this article is available at http://advances.sciencemag.org/cgi/content/full/6/2/eaax4177/DC1

Supplementary Materials and Methods

Fig. S1. Comparisons of the simulation skill for the ENSO-related precipitation and SST anomalies between ESPPE and CMIP5 models by Taylor diagrams.

Fig. S2. Budget analysis of the moisture (eq. S1).

Fig. S3. Linear decomposition of change in vertically integrated vertical advection of climatological humidity by anomalous vertical motion under global warming.

Fig. S4. Derivation of deep and shallow modes of vertical motions and horizontal convergences over the tropical oceans (20°S to 20°N).

Fig. S5. Changes in ENSO-driven boundary-layer wind (vector, m s^{-1}) and convergence anomalies (shading, 10^{-6} s^{-1}) under global warming estimated by the MLM.

Fig. S6. Budget analysis of the MSE (eq. S6).

Fig. S7. Physical processes responsible for the change in the vertically integrated vertical advection of mean MSE by anomalous vertical motions associated with the change in deep-mode amplitude ($\Delta\sigma_d'\langle\Omega_d\partial_p\bar{h}\rangle$) over the equatorial CEP.

Fig. S8. Decomposition of the change in vertically integrated horizontal advection of mean moist enthalpy by ENSO-related wind anomalies ($\Delta\langle-\vec{u}'\nabla_h\bar{K}\rangle$).

Fig. S9. Simulated changes in the ENSO-driven D(0)JF(1)-mean precipitation and SST anomalies under global warming in 31 CMIP5 models.

Fig. S10. Scatter diagram for changes in divergence of meridional gradient of SST anomalies averaged in 4°N to 4°S, 170° to 120°W (ordinate axis) versus change in local surface convergence anomalies (abscissa axis) derived from the 31 CMIP5 models.

References (*62*–*68*)

REFERENCES AND NOTES

1. J. Bjerknes, Atmospheric teleconnections from the equatorial Pacific. *Mon. Weather Rev.* **97**, 163–172 (1969).
2. S. G. Philander, *El Niño, La Niña, and the Southern Oscillation* (Academic, 1990).
3. J. D. Neelin, D. S. Battisti, A. C. Hirst, F.-F. Jin, Y. Wakata, T. Yamagata, S. E. Zebiak, ENSO theory. *J. Geophys. Res.* **103**, 14261–14290 (1998).
4. M. J. McPhaden, S. E. Zebiak, M. H. Glantz, ENSO as an integrating concept in Earth science. *Science* **314**, 1740–1745 (2006).
5. A. Timmermann, S.-I. An, J.-S. Kug, F.-F. Jin, W. Cai, A. Capotondi, K. M. Cobb, M. Lengaigne, M. J. McPhaden, M. F. Stuecker, K. Stein, A. T. Wittenberg, K.-S. Yun, T. Bayr, H.-C. Chen, Y. Chikamoto, B. Dewitte, D. Dommenget, P. Grothe, E. Guilyardi, Y.-G. Ham, M. Hayashi, S. Ineson, D. Kang, S. Kim, W. Kim, J.-Y. Lee, T. Li, J.-J. Luo, S. McGregor, Y. Planton, S. Power, H. Rashid, H.-L. Ren, A. Santoso, K. Takahashi, A. Todd, G. Wang, G. Wang, R. Xie, W.-H. Yang, S.-W. Yeh, J. Yoon, E. Zeller, X. Zhang, El Niño–Southern Oscillation complexity. *Nature* **559**, 535–545 (2018).
6. P. W. Glynn, W. H. De Weerdt, Elimination of two reef-building hydrocorals following the 1982-83 El Niño warming event. *Science* **253**, 69–71 (1991).
7. M. C. Bove, J. J. O'Brien, J. B. Eisner, C. W. Landsea, X. Niu, Effect of El Niño on US landfalling hurricanes, revisited. *Bull. Am. Meteorol. Soc.* **79**, 2477–2482 (1998).
8. G. D. Bell, M. S. Halpert, C. F. Ropelewski, V. E. Kousky, A. V. Douglas, R. C. Schnell, M. E. Gelman, Climate assessment for 1998. *Bull. Am. Meteorol. Soc.* **80**, S1–S48 (1998).
9. S.-W. Yeh, W. Cai, S.-K. Min, M. J. McPhaden, D. Dommenget, B. Dewitte, J.-S. Kug, ENSO atmospheric teleconnections and their response to greenhouse gas forcing. *Rev. Geophys.* **56**, 185–206 (2018).
10. M. Collins, S.-I. An, W. Cai, A. Ganachaud, E. Guilyardi, F.-F. Jin, M. Jochum, M. Lengaigne, S. Power, A. Timmermann, G. A. Vecchi, A. T. Wittenberg, The impact of global warming on the tropical Pacific Ocean and El Nïno. *Nat. Geosci.* **3**, 391–397 (2010).
11. G. A. Vecchi, A. T. Wittenberg, El Niño and our future climate: Where do we stand? *Wiley Interdiscip. Rev. Clim. Chang.* **1**, 260–270 (2010).
12. P. N. DiNezio, B. P. Kirtman, A. C. Clement, S.-K. Lee, G. A. Vecchi, A. T. Wittenberg, Mean climate controls on the simulated response of ENSO to increasing greenhouse gases. *J. Clim.* **25**, 7399–7420 (2012).
13. S. L. Stevenson, Significant changes to ENSO strength and impacts in the twenty-first century: Results from CMIP5. *Geophys. Res. Lett.* **39**, L17703 (2012).
14. M. Watanabe, J.-S. Kug, F.-F. Jin, M. Collins, M. Ohba, A. T. Wittenberg, Uncertainty in the ENSO amplitude change from the past to the future. *Geophys. Res. Lett.* **39**, L20703 (2012).
15. S. T. Kim, W. Cai, F.-F. Jin, A. Santoso, L. Wu, E. Guilyardi, S.-I. An, Response of El Niño sea surface temperature variability to greenhouse warming. *Nat. Clim. Change* **4**, 786–790 (2014).
16. W. Cai, A. Santoso, G. Wang, S.-W. Yeh, S.-I. An, K. M. Cobb, M. Collins, E. Guilyardi, F.-F. Jin, J.-S. Kug, M. Lengaigne, M. J. McPhaden, K. Takahashi, A. Timmermann, G. Vecchi, M. Watanabe, L. Wu, ENSO and greenhouse warming. *Nat. Clim. Change* **5**, 849–859 (2015).
17. Y.-G. Ham, J.-S. Kug, ENSO amplitude changes due to greenhouse warming in CMIP5: Role of mean tropical precipitation in the twentieth century. *Geophys. Res. Lett.* **43**, 422–430 (2016).
18. W. Cai, G. Wang, B. Dewitte, L. Wu, A. Santoso, K. Takahashi, Y. Yang, A. Carréric, M. J. McPhaden, Increased variability of eastern Pacific El Niño under greenhouse warming. *Nature* **564**, 201–206 (2018).
19. S. B. Power, F. Delage, C. T. Chung, G. Kociuba, K. Keay, Robust twenty-first century projections of El Niño and related precipitation variability. *Nature* **502**, 541–547 (2014).
20. W. Cai, S. Borlace, M. Lengaigne, P. V. Rensch, M. Collins, G. Vecchi, A. Timmermann, A. Santoso, M. J. Mcphaden, L. Wu, M. H. England, G. Wang, E. Guilyardi, F.-F. Jin, Increasing frequency of extreme El Niño events due to greenhouse warming. *Nat. Clim. Change* **4**, 111–116 (2014).
21. P. Huang, S. P. Xie, Mechanisms of change in ENSO-induced tropical Pacific rainfall variability in a warming climate. *Nat. Geosci.* **8**, 922–926 (2015).
22. P. Huang, Time-varying response of ENSO-induced tropical pacific rainfall to global warming in CMIP5 models. Part I: Multimodel ensemble results. *J. Clim.* **29**, 5763–5778 (2016).
23. P. Huang, Time-varying response of ENSO-induced tropical pacific rainfall to global warming in CMIP5 models. Part II: Intermodel uncertainty. *J. Clim.* **30**, 595–608 (2017).
24. S. B. Power, F. P. D. Delage, C. T. Y. Chung, H. Ye, B. F. Murphy, Humans have already increased the risk of major disruptions to Pacific rainfall. *Nat. Commun.* **8**, 14368 (2017).
25. S. B. Power, F. P. D. Delage, El Niño-Southern oscillation and associated climatic conditions around the world during the latter half of the twenty-first century. *J. Clim.* **31**, 6189–6207 (2018).
26. C. J. W. Bonfils, B. D. Santer, T. J. Phillips, K. Marvel, L. R. Leung, C. Doutriaux, A. Capotondi, Relative contributions of mean-state shifts and ENSO-driven variability to precipitation changes in a warming climate. *J. Clim.* **28**, 9997–10013 (2015).
27. C. T. Y. Chung, S. B. Power, Modelled impact of global warming on ENSO-driven precipitation changes in the tropical Pacific. *Clim. Dyn.* **47**, 1303–1323 (2016).
28. T. Bayr, D. Dommenget, T. Martin, S. B. Power, The eastward shift of the Walker Circulation in response to global warming and its relationship to ENSO variability. *Clim. Dyn.* 2747–2763 (2014).
29. G. A. Meehl, H. Teng, Multi-model changes in El Niño teleconnections over North America in a future warmer climate. *Clim. Dyn.* **29**, 779–790 (2007).
30. W. A. Müller, E. Roeckner, ENSO teleconnections in projections of future climate in ECHAM5/MPI-OM. *Clim. Dyn.* **31**, 533–549 (2008).
31. J.-S. Kug, S.-I. An, Y.-G. Ham, I.-S. Kang, Changes in El Niño and La Niña teleconnections over North Pacific-America in the global warming simulations. *Theor. Appl. Climatol.* **100**, 275–282 (2010).
32. Z.-Q. Zhou, S.-P. Xie, X.-T. Zheng, Q. Liu, H. Wang, Global warming-induced changes in El Niño teleconnections over the North Pacific and North America. *J. Clim.* **27**, 9050–9064 (2014).
33. S. J. Perry, S. McGregor, A. Sen Gupta, M. H. England, Future changes to El Niño–Southern Oscillation temperature and precipitation teleconnections. *Geophys. Res. Lett.* **44**, 10608–10616 (2017).
34. B. Wu, T. Zhou, T. Li, Atmospheric dynamic and thermodynamic processes driving the western north Pacific anomalous anticyclone during El Niño. Part I: Maintenance Mechanisms. *J. Clim.* **30**, 9637–9650 (2017).
35. T. Bayr, M. Latif, D. Dommenget, C. Wengel, J. Harlaß, W. Park, Mean-state dependence of ENSO atmospheric feedbacks in climate models. *Clim. Dynam.* **50**, 3171–3194 (2018).
36. T. Bayr, C. Wengel, M. Latif, D. Dommenget, J. Lübbecke, W. Park, Error compensation of ENSO atmospheric feedbacks in climate models and its influence on simulated ENSO dynamics. *Clim. Dyn.* 155–172 (2018).
37. T. Bayr, D. I. V. Domeisen, C. Wengel, The effect of the equatorial Pacific cold SST bias on simulated ENSO teleconnections to the North Pacific and California. *Clim. Dyn.* 3771–3789 (2019).
38. W. Jiang, G. Huang, P. Huang, K. Hu, Weakening of northwest Pacific anticyclone anomalies during Post-El Niño summers under global warming. *J. Clim.* **31**, 3539–3555 (2018).
39. L. E. Back, C. S. Bretherton, Geographic variability in the export of moist static energy and vertical motion profiles in the tropical Pacific. *Geophys. Res. Lett.* **33**, L17810 (2006).
40. L. E. Back, C. S. Bretherton, A simple model of climatological rainfall and vertical motion patterns over the tropical oceans. *J. Clim.* **22**, 6477–6497 (2009).
41. L. E. Back, C. S. Bretherton, On the relationship between SST gradients, boundary layer winds, and convergence over the tropical oceans. *J. Clim.* **22**, 4182–4196 (2009).
42. R. S. Lindzen, S. Nigam, On the role of sea surface temperature gradients in forcing low-level winds and convergence in the tropics. *J. Atmos. Sci.* **44**, 2418–2436 (1987).
43. L. P. McCreary JP Jr., P. Lu, Interaction between the subtropical and equatorial ocean circulations: The subtropical cell. *J. Phys. Oceanogr.* **24**, 466–497 (1994).
44. W. Zhang, J. Li, F.-F. Jin, Spatial and temporal features of ENSO meridional scales. *Geophys. Res. Lett.* **36**, L15605 (2009).
45. W. Zhang, F.-F. Jin, Improvements in the CMIP5 simulations of ENSO-SSTA meridional width. *Geophys. Res. Lett.* **39**, L23704 (2012).

46. W. Zhang, F.-F. Jin, J. X. Zhao, J. Li, On the bias in simulated ENSO SSTA meridional widths of CMIP3 models. *J. Clim.* **26**, 3173–3186 (2013).
47. L. Chen, T. Li, Y. Yu, Causes of strengthening and weakening of ENSO amplitude under global warming in four CMIP5 models. *J. Clim.* **28**, 3250–3274 (2015).
48. L. Chen, T. Li, Y. Yu, S. K. Behera, A possible explanation for the divergent projection of ENSO amplitude change under global warming. *Clim. Dyn.* **49**, 3799–3811 (2017).
49. F. Liu, Y. Luo, J. Lu, X. Wan, Response of the tropical Pacific Ocean to El Niño versus global warming. *Clim. Dyn.* **48**, 935–956 (2017).
50. J. D. Neelin, I. M. Held, Modeling tropical convergence based on the moist static energy budget. *Mon. Weather Rev.* **115**, 3–12 (1987).
51. B. Wu, T. Zhou, T. Li, Atmospheric dynamic and thermodynamic processes driving the western north Pacific anomalous anticyclone during El Niño. Part II: Formation processes. *J. Clim.* **30**, 9637–9650 (2017).
52. R. H. Weisberg, C. Wang, A western Pacific oscillator paradigm for the El Niño-Southern Oscillation. *Geophys. Res. Lett.* **24**, 779–782 (1997).
53. R. H. Weisberg, C. Wang, Slow variability in the equatorial west-central Pacific in relation to ENSO. *J. Clim.* **10**, 1998–2017 (1997).
54. B. Wang, R. Wu, R. Lukas, S.-I. An, A possible mechanism for ENSO turnabouts, in *Dynamics of Atmospheric General Circulation and Climate* (China Meteorological Press, 2001).
55. B. Wu, T. Li, T. Zhou, Relative contributions of the Indian Ocean and local SST anomalies to the maintenance of the western North pacific anomalous anticyclone during the El Niño decaying summer. *J. Clim.* **23**, 2974–2986 (2010).
56. M. Chen, X. Shen, Relative roles of dynamic and thermodynamic processes in causing evolution asymmetry between El Niño and La Niña. *J. Clim.* **29**, 2201–2220 (2016).
57. J. M. Murphy, B. B. B. Booth, M. Collins, G. R. Harris, D. M. H. Sexton, M. J. Webb, A methodology for probabilistic predictions of regional climate change from perturbed physics ensembles. *Philos. Trans. R. Soc. A* **365**, 1993–2028 (2007).
58. J. M. Murphy, B. B. B. Booth, C. A. Boulton, R. T. Clark, G. R. Harris, J. A. Lowe, D. M. H. Sexton, Transient climate changes in a perturbed parameter ensemble of emissions-driven earth system model simulations. *Clim. Dyn.* **43**, 2855–2885 (2014).
59. F. H. Lambert, M. Collins, G. R. Harris, J. M. Murphy, D. M. H. Sexton, B. B. B. Booth, Interactions between perturbations to different Earth system components simulated by a fully-coupled climate model. *Clim. Dyn.* **41**, 3055–3072 (2013).
60. J. D. Neelin, *Moist Dynamics of Tropical Convection Zones in Monsoons, Teleconnections and Global Warming. The Global Circulation of the Atmosphere*, T. Schneider, A. H. Sobel, Eds. (Princeton Univ. Press, 2007), pp. 267–301.
61. B. Wu, T. Zhou, Relationships between ENSO and the East Asian–western North Pacific monsoon: Observations versus 18 CMIP5 models. *Clim. Dyn.* **46**, 729–743 (2016).
62. B. Stevens, J. Duan, J. C. McWilliams, M. Münnich, J. D. Neelin, Entrainment, Rayleigh friction, and boundary layer winds over the tropical Pacific. *J. Clim.* **15**, 30–44 (2002).
63. R. F. Adler, G. J. Huffman, A. Chang, R. Ferraro, P. P. Xie, J. Janowiak, B. Rudolf, U. Schneider, S. Curtis, D. Bolvin, A. Gruber, J. Susskind, P. Arkin, E. Nelkin, The version-2 global precipitation climatology project (GPCP) monthly precipitation analysis (1979-present). *J. Hydrometeorol.* **4**, 1147–1167 (2003).
64. N. A. Rayner, D. E. Parker, E. B. Horton, C. K. Folland, L. V. Alexander, D. P. Rowell, E. C. Kent, A. Kaplan, Global analyses of sea surface temperature, sea ice, and night marine air temperature since the late nineteenth century. *J. Geophys. Res.* **108**, 4407 (2003).
65. G. A. Vecchi, B. J. Soden, Global warming and the weakening of the tropical circulation. *J. Clim.* **20**, 4316–4340 (2007).
66. H. Su, J. D. Neelin, Teleconnection mechanism for tropical Pacific descent anomalies during El Niño. *J. Atmos. Sci.* **59**, 2694–2712 (2002).
67. C. S. Bretherton, A. H. Sobel, A simple model of a convectively-coupled Walker circulation using the weak temperature gradient approximation. *J. Clim.* **15**, 2907–2920 (2002).
68. J. D. Neelin, H. Su, Moist teleconnection mechanisms for the tropical South American and Atlantic sector. *J. Clim.* **18**, 3928–3950 (2005).

Acknowledgments: We thank T. Bayr and the other two anonymous reviewers for their constructive comments that helped greatly to improve the original manuscript. **Funding:** B.W. and Z.Y. were supported by the NSFC (grant 41661144009), the National Key Research and Development Program of China (grant nos. 2017YFA0603802 and 2018YFA0606301), and the GOTHAM International Cooperative Project. T.L. was supported by NSFC grant 41630423, NSF AGS-1565653, and NOAA NA18OAR4310298. M.C., R.C., and J.M. were supported by the UK-China Research and Innovation Partnership Fund through the Met Office Climate Science for Service Partnership (CSSP) China as part of the Newton Fund. T.Z. was supported by the Strategic Priority Research Programme of Chinese Academy of Sciences (grant XDA20060102). **Author contributions:** B.W. designed this study. B.W. and Z.Y. wrote the initial version of the paper. Z.Y. performed the model output analysis and generated all figures. All authors contributed to interpreting results, discussion of the associated dynamics, and improvement of this paper. **Competing interests:** The authors declare that they have no competing interests. **Data and materials availability:** All data needed to evaluate the conclusions in the paper are present in the paper and/or the Supplementary Materials. Additional data related to this paper may be requested from the authors.

Submitted 21 March 2019
Accepted 14 November 2019
Published 8 January 2020
10.1126/sciadv.aax4177

Citation: Z. Yan, B. Wu, T. Li, M. Collins, R. Clark, T. Zhou, J. Murphy, G. Tan, Eastward shift and extension of ENSO-induced tropical precipitation anomalies under global warming. *Sci. Adv.* **6**, eaax4177 (2020).